



Seismic response for an isosceles triangle hill subjected to anti-plane shear waves

Yunqiu Song¹ · Xinzhu Li¹ · Zailin Yang^{1,2} · Yong Yang^{1,2} · Menghan Sun¹

Received: 12 July 2020 / Accepted: 12 April 2021 / Published online: 28 April 2021

© The Author(s), under exclusive licence to Springer-Verlag GmbH Germany, part of Springer Nature 2021

Abstract

This paper presents an exact, analytical solution to the boundary value problem of the anti-plane (SH) waves scattering by an isosceles triangle hill on an elastic half-space by using the wavefunction expansion method. An appropriate region-matching technique is introduced to divide the half-space containing a triangle hill into two subregions. Then, the wavefield expression of each subregion is constructed in terms of an infinite series in two coordinate systems, respectively. Furthermore, a Graf's addition formula is derived to unify the coordinate system and solve the unknown coefficients in the wave functions. Finally, numerical results are calculated to illustrate the effects on ground motion due to the existence of an isosceles triangle hill. This paper revises the existing analytical methods, and aims to provide a benchmark for numerical method verification and a reference for engineering practice.

Keywords Analytic solution · Isosceles triangle hill · Seismic amplification · SH waves scattering

1 Introduction

The impact of local topography on ground motion is one of the key topics of concern in the field of earthquake engineering. It is indicated by theoretical research and damage experience that the ground motions of canyons or hills are stronger than that of the plane. The ground motion responses of different forms of topography are diverse when an earthquake occurs, so a remarkable amount of work has been done on the scattering of seismic waves from local topography of various shapes.

To reveal the amplification effects due to topography of the canyon, semi-cylindrical canyon was the first form to be considered in terms of analytical solution [16]. The research on the scattering of SH wave by semi-circular

canyon provided convenience for the following studies on other shaped canyons. By introducing a Graf's addition formula and combining with the expression of scattering wave excited by the circular arc boundary, the ground motion of the circular arc canyon topography could be further studied [24]. For the concave topography with more complex geometry, it is difficult to give the scattered wave field excited by the terrain boundary. The introduction of auxiliary boundary is an effective way to solve this kind of problem. Based on the region-matching technique (RMT), Tsaur and Chang [17] adopted the wave function expansion method and the fractional Bessel function to give the analytical solution of the scattering of SH wave by a shallow symmetrical V-shaped canyon. The combination of fractional-order Bessel function and RMT had been proved to be feasible in the ground motion investigation of the canyon topography with complex shapes [3, 4, 6, 7, 19, 27]. In addition to analytical methods, many methods such as semi-analytical method [5], boundary element method [23] and hybrid method [13] can be adopted to analyze the influence of canyon and valley topography on seismic wave propagation.

Compared with the concave topography, there are much fewer analytical methods to study the ground motion of hills. Yuan and Men [26] had proposed an analytical

✉ Zailin Yang
yangzailin00@163.com

✉ Menghan Sun
sunmenghan163@hrbeu.edu.cn

¹ College of Aerospace and Civil Engineering, Harbin Engineering University, Harbin, China

² Key Laboratory of Advanced Material of Ship and Mechanics, Ministry of Industry and Information Technology, Harbin Engineering University, Harbin, China

method to solve the scattering problem of SH waves by a semi-cylindrical hill. Although an effective partitioning method is proposed, the results are only applicable to low-frequency incident SH waves due to solving errors. To get high precision numerical results, Lee et al. [10] proposed an improved analytical series solution adopting a cosine half-range expansion to meet the boundary conditions. For convex topography with circular arc cross section, Tsaur and Chang [18] found that series solution of [25] was in error due to unsuitable connection between the domain decomposition and the expression of corresponding wavefield and rederived the wave field expressions based on the RMT by introducing a semi-circular auxiliary boundary. Similarly, by establishing the elliptic coordinate system and introducing the Mathieu function, the ground motion of a semi elliptical hill under incident SH waves was studied [2, 9, 11]. In addition to the hills with circular and elliptical boundaries, ground motions for hills with slopes had also been considered. Hayir and Todorovska [8] attempted to get the series solution for the isosceles triangle topography by wavefunctions expansion method. Unfortunately, their calculated results did not coincide with the numerical results of Sánchez-Sesma et al. [15]. By introducing fractional Bessel function, Qiu and Liu [12] constructed the displacement field expression which satisfies the stress-free condition of triangle boundary rigorously. However, the numerical results [9, Sect. 5] were correct just under very low wave frequency incidence and could only be applied to the case of shallow hill.

In this paper, the analytic solution of SH wave scattering by an isosceles triangular hill is presented. The proposed method is not only applicable to hills of any height, but also can be used to calculate the numerical results of good convergence in the case of high incident wave frequency. Although the ground motions of more geometrically complex hill have been studied analytically [14, 22], it is necessary to give exact analytical results for the triangular hill as a typical convex topography, which can provide references for engineering practice and serve as a benchmark for comparison of numerical methods. In addition, investigating simple local topography under inhomogeneous geological conditions has been a hot topic in recent years [20, 21, 28, 29]. The research methods and solution ideas proposed in this paper provide a theoretical basis for subsequent studies combining complex geology. Furthermore, by changing the medium parameters, the mechanical model can be established to study the rock-soil interaction, and the dynamic response of dam foundation and soil can be studied by changing the form of triangular bottom boundary.

In Sect. 2 of this paper, the isosceles triangle hill is modeled and the partition method of this problem and the related parameters are explained. We rederived the wave field expressions in each subregion and establish the infinite

algebraic equations for programming in Sect. 3. Then, in Sect. 4, the convergence and correctness of the results are verified, and the steady-state responses with different parameters are analyzed. Finally, the methods adopted in this paper and some important results are summarized in Sect. 5.

2 Model

The two-dimensional model studied in this paper is shown in Fig. 1 which represents an elastic, isotropic and homogeneous half space (with shear modulus μ and shear wave velocity c) supporting an isosceles triangle hill of height h and half-width a . The origin of the global coordinate systems (x_1, y_1) and (r_1, θ_1) is set at the hill top, while that of the local coordinate systems (x_2, y_2) and (r_2, θ_2) is set at the center of the hill bottom. The angle θ_1 and θ_2 are measured anticlockwise from the vertical y_1 -axis and y_2 -axis, respectively. The angles between the hillsides and the vertical y_1 -axis are $-\beta$ and β , which means the central angle of the hill top is 2β , ranging from 0 to π . Based on the region-matching technique, a circular arc auxiliary boundary S_a is introduced to divide the half-space into two subregions. Region I involves an enclosed sector area and region II is a semi-infinite region with a circular arc canyon. Half of the hill span is a , which means the radius of the circular arc auxiliary boundary S_a is $a/\sin \beta$.

3 Theoretical formulation

All the displacement w_j ($j = 1, 2$) within region I and region II must satisfy the two-dimensional wave equation

$$\frac{\partial^2 w_j}{\partial r_j^2} + \frac{1}{r_j} \frac{\partial w_j}{\partial r_j} + \frac{1}{r_j^2} \frac{\partial^2 w_j}{\partial \theta_j^2} = \frac{1}{c^2} \frac{\partial^2 w_j}{\partial t^2} \quad (1)$$

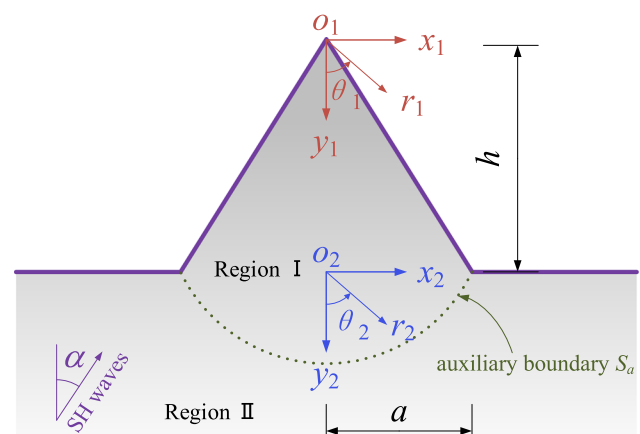


Fig. 1 Model of the isosceles triangle hill

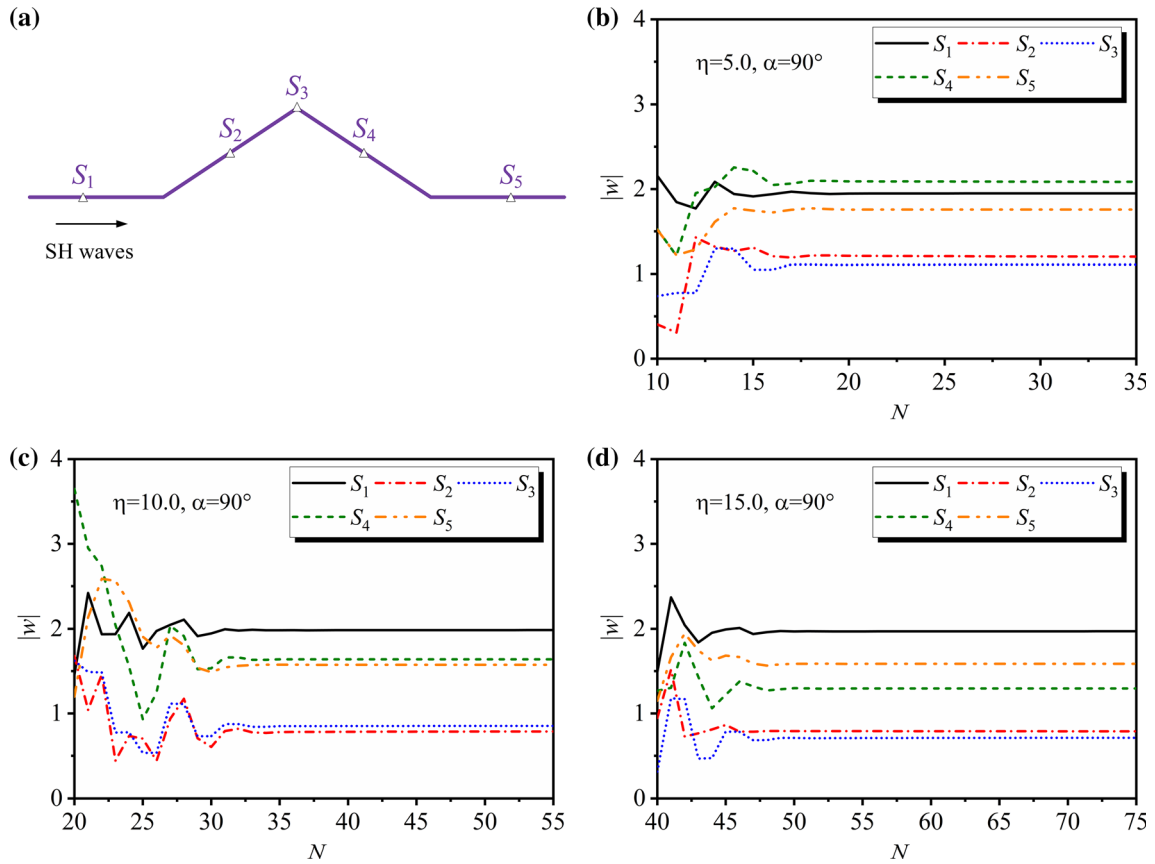


Fig. 2 Convergence of displacement amplitudes at five positions with increasing N : **a** five selected positions; **b** $\eta = 5.0$; **c** $\eta = 10.0$; **d** $\eta = 15.0$

By letting

$$w(r_j, \theta_j, t) = w(r_j, \theta_j) \exp(-i\omega t) \tag{2}$$

and omitting the term $\exp(-i\omega t)$, the steady-state anti-plane wave motion equation can be obtained

$$\nabla^2 w_j + k^2 w_j = 0, \tag{3}$$

where ∇^2 is the Laplacian and $k = \omega/c$ is the shear wave number.

The zero-stress boundary conditions on the horizontal ground surface and the hill surface are

$$\tau_{\theta_1 z_1}^{(1)} = \frac{\mu}{r_1} \frac{\partial w_1}{\partial \theta_1} = 0, \theta_1 = \pm\beta, 0 \leq r_1 \leq b \tag{4}$$

$$\tau_{\theta_2 z_2}^{(2)} = \frac{\mu}{r_2} \frac{\partial w_2}{\partial \theta_2} = 0, \theta_2 = \pm \frac{\pi}{2}, r_2 > a \tag{5}$$

Since the auxiliary boundary is introduced to divide the model into two regions, the continuity conditions of displacement and stress at the auxiliary boundary must also be satisfied. The matching conditions on the auxiliary boundary can be written as

$$w_1(r_1, \theta_1) = w_2(r_1, \theta_1), r_1 = b, -\beta \leq \theta_1 \leq \beta, \tag{6}$$

$$\tau_{r_1 z}^{(1)}(r_1, \theta_1) = \tau_{r_1 z}^{(2)}(r_1, \theta_1), r_1 = b, -\beta \leq \theta_1 \leq \beta, \tag{7}$$

where $\tau_{r_1 z}^{(1)}(r_1, \theta_1) = \mu \frac{\partial w_1}{\partial r_1}$ and $\tau_{r_1 z}^{(2)}(r_1, \theta_1) = \mu \frac{\partial w_2}{\partial r_1}$.

The total wave in region II can be split into the scattered wave w^s by the circular arc auxiliary boundary S_a and the free-field displacement w^f , that is

$$w_1 = w^f + w^s, \tag{8}$$

where the free-field displacement w^f is expressed as

$$w^f(r_2, \theta_2) = \exp[-ikr_2 \cos(\theta_2 + \alpha)] + \exp[ikr_2 \cos(\theta_2 - \alpha)], \tag{9}$$

Note that this expression is written in the coordinate system (r_2, θ_2) , and for later computation, it should be converted to the coordinate system (r_1, θ_1) . According to the transformation relationship between the two coordinate systems, $x_1 = x_2$ and $y_1 = y_2 + h$, Eq. (9) can be re-expressed in the coordinate systems (r_1, θ_1) as

$$w^f(r_1, \theta_1) = \exp(ikh \cos \alpha) \exp[-ikr_1 \cos(\theta_1 + \alpha)] + \exp(-ikh \cos \alpha) \exp[ikr_1 \cos(\theta_1 - \alpha)] \tag{10}$$

Employing the Jacobi–Anger expansion [1],

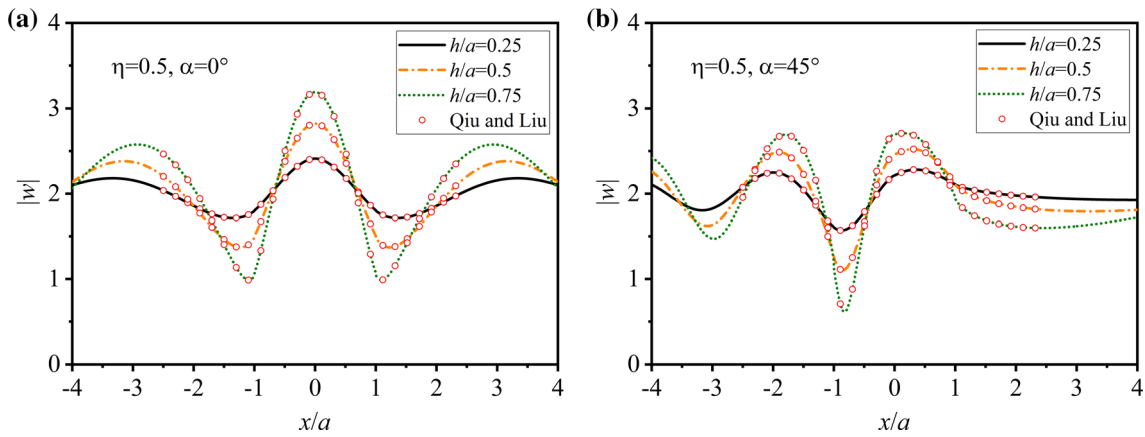


Fig. 3 Comparison between our results for different hill height at $\eta = 0.5$ and those of Qiu and Liu: **a** $\alpha = 0^\circ$; **b** $\alpha = 45^\circ$

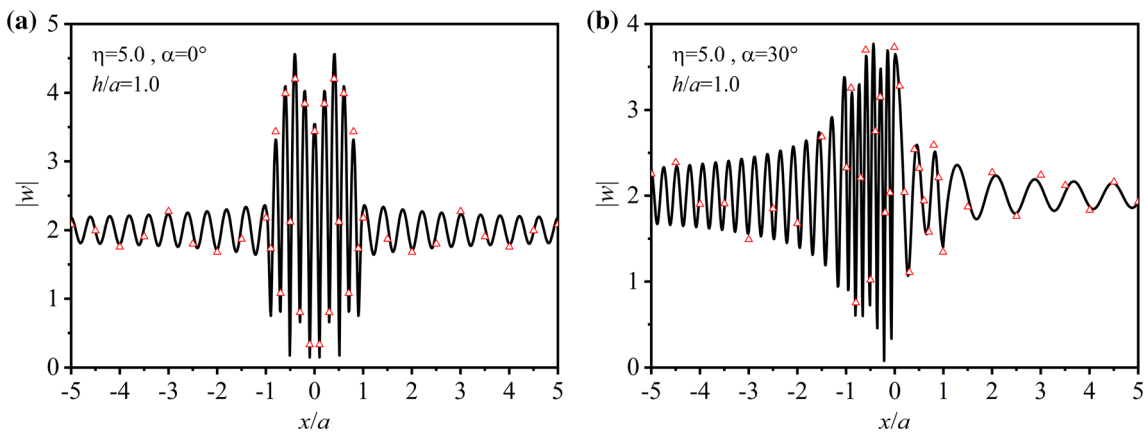


Fig. 4 Surface displacement amplitude versus x/a with $h/a = 1.0$ at $\eta = 5.0$: **a** $\alpha = 0^\circ$; **b** $\alpha = 30^\circ$. The solid lines show the results from the series solution and the scatter points show the results from the FEM

$$\exp(\pm ikr \cos \theta) = \sum_{n=0}^{\infty} \varepsilon_n (\pm i)^n J_n(kr) \cos n\theta, \tag{11}$$

where ε_n is the Neumann factor ($\varepsilon_0 = 1$; $\varepsilon_n = 2$, $n > 0$) and $J_n(\cdot)$ is the Bessel function with order n . Equation (10) is expressed as

$$w^f(r_1, \theta_1) = \sum_{n=0}^{\infty} J_n(kr_1) (a_n \cos n\theta_1 + b_n \sin n\theta_1), \tag{12}$$

$$-\beta \leq \theta_1 \leq \beta$$

in which

$$a_n = \varepsilon_n [(-i)^n \exp(ikh \cos \alpha) + i^n \exp(-ikh \cos \alpha)] \cos n\alpha \tag{13}$$

$$b_n = \varepsilon_n [(-i)^n \exp(ikh \cos \alpha) + i^n \exp(-ikh \cos \alpha)] \sin n\alpha \tag{14}$$

Due to the existence of auxiliary boundary S_a , there is scattered wave in region I. It is given as

$$w^s(r_2, \theta_2) = \sum_{n=0}^{\infty} A_n H_{2n}^{(1)}(kr_2) \cos 2n\theta_2 + \sum_{n=0}^{\infty} B_n H_{2n+1}^{(1)}(kr_2) \sin(2n+1)\theta_2, \tag{15}$$

where A_n and B_n are unknown complex coefficients, $H_n^{(1)}(\cdot)$ denotes the Hankel function of the first kind with order n .

It is convenient further on to represent w^s also in the coordinate system (r_1, θ_1) . The application of the Graf addition formula [1] gives

$$w^s(r_1, \theta_1) = \sum_{n=0}^{\infty} A_n \sum_{m=0}^{\infty} I_{m,2n}^c H_m^{(1)}(kr_1) \cos m\theta_1 + \sum_{n=0}^{\infty} B_n \sum_{m=0}^{\infty} I_{m,2n+1}^s H_m^{(1)}(kr_1) \sin m\theta_1, \tag{16}$$

where

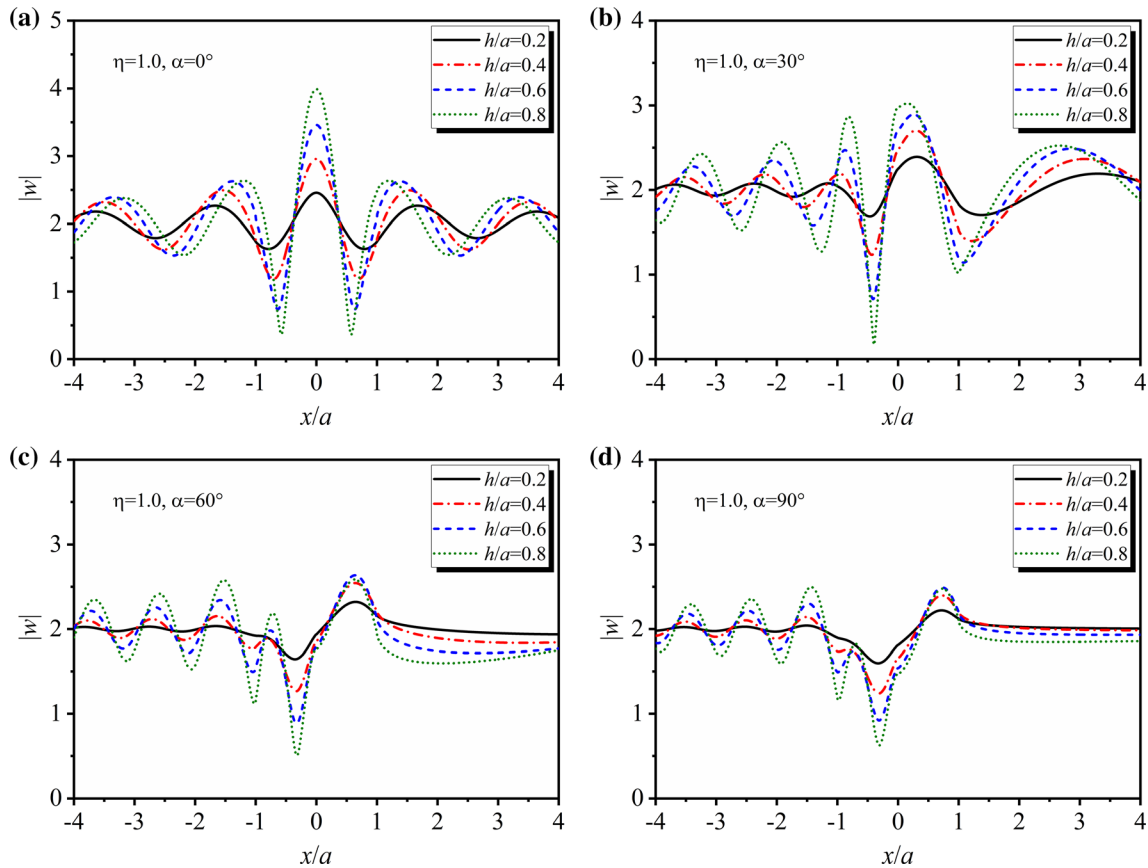


Fig. 5 Amplitudes of surface displacement versus x/a at $\eta = 1.0$ for various incident angles: shallow hill

$$I_{m,n}^c = (-1)^n \frac{\epsilon_m}{2} [(-1)^n J_{m-n}(kd) + J_{m+n}(kd)] \quad (17)$$

$$I_{m,n}^s = (-1)^{n+1} \frac{\epsilon_m}{2} [J_{m+n}(kd) - (-1)^n J_{m-n}(kd)] \quad (18)$$

In the enclosed region II, the standing wave expression w_2 is given by

$$\begin{aligned} w_2 &= w^t(r_1, \theta_1) \\ &= \sum_{n=0}^{\infty} C_n J_{2np}(kr_1) \cos 2np\theta_1 \\ &\quad + \sum_{n=0}^{\infty} D_n J_{(2n+1)p}(kr_1) \sin(2n+1)p\theta_1 \end{aligned} \quad (19)$$

in which C_n and D_n are unknown complex coefficients, $p = \pi/(2\beta)$ is a fractional factor missed to consider in Ref. [8], which is used to make the expression of standing wave automatically satisfy the stress-free condition of hill surface.

Notice that the unknown coefficients A_n , B_n , C_n and D_n need to be determined according to Eqs. (6) and (7). Multiplying both sides of Eqs. (6) and (7) by cosine/sine functions, and integrating over the range of $[-\beta, \beta]$ gives

$$\begin{aligned} & - \sum_{n=0}^{\infty} A_n \sum_{m=0}^{\infty} I_{m,2n}^c H_m^{(1)}(kb) U_{m,l} + \sum_{n=0}^{\infty} C_n J_{2np}(kb) U_{2np,l} \\ &= \sum_{n=0}^{\infty} a_n J_n(kb) U_{n,l}, \quad l = 0, 1, \dots, \end{aligned} \quad (20)$$

$$\begin{aligned} & - \sum_{n=0}^{\infty} A_n \sum_{m=0}^{\infty} I_{m,2n}^s H_m^{(1)'}(kb) U_{m,l} + \sum_{n=0}^{\infty} C_n J'_{2np}(kb) U_{2np,l} \\ &= \sum_{n=0}^{\infty} a_n J'_n(kb) U_{n,l}, \quad l = 0, 1, \dots, \end{aligned} \quad (21)$$

$$\begin{aligned} & - \sum_{n=0}^{\infty} B_n \sum_{m=0}^{\infty} I_{m,2n+1}^s H_m^{(1)}(kb) V_{m,l} \\ &+ \sum_{n=0}^{\infty} D_n J_{(2n+1)p}(kb) V_{(2n+1)p,l} \\ &= \sum_{n=0}^{\infty} b_n J_n(kb) V_{n,l}, \quad l = 0, 1, \dots, \end{aligned} \quad (22)$$

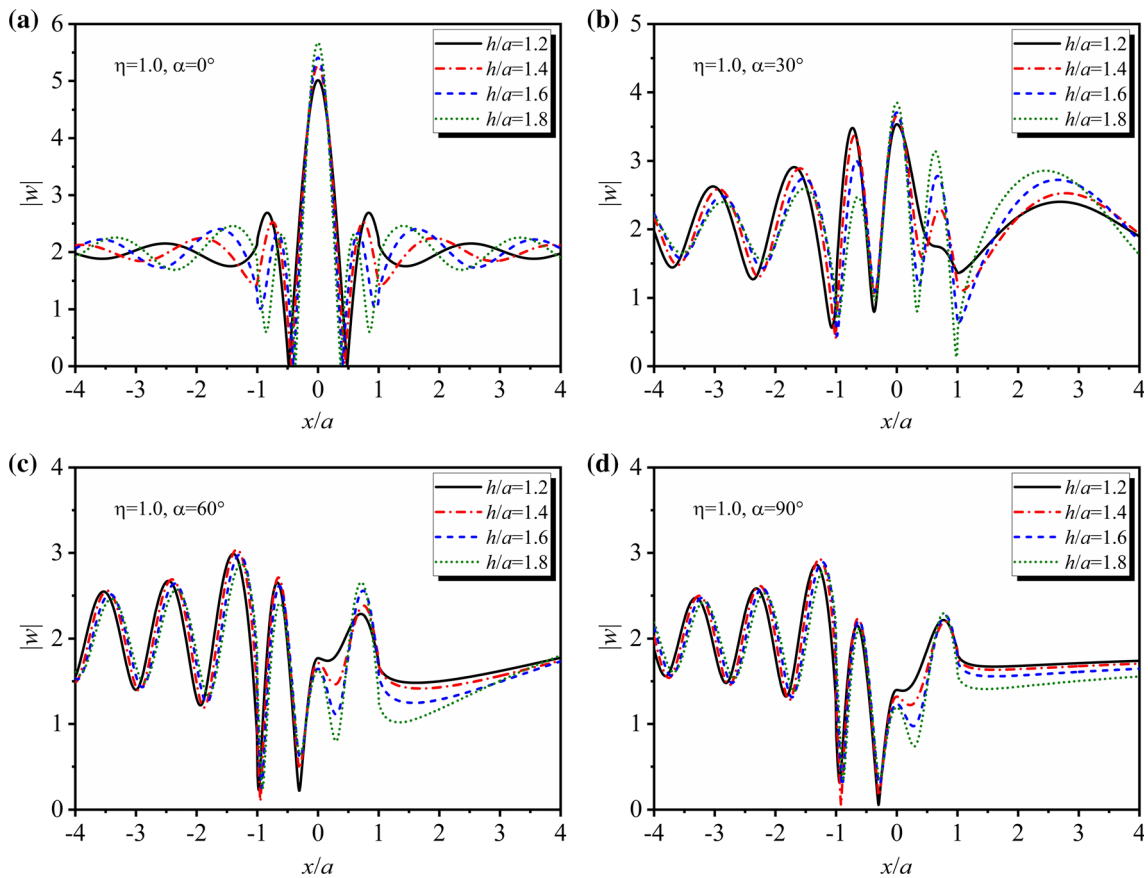


Fig. 6 Amplitudes of surface displacement versus x/a at $\eta = 1.0$ for various incident angles: deep hill

$$\begin{aligned}
 & - \sum_{n=0}^{\infty} B_n \sum_{m=0}^{\infty} I_{m,2n+1}^s H_m^{(1)'}(kb) V_{m,l} \\
 & + \sum_{n=0}^{\infty} D_n J'_{(2n+1)p}(kb) V_{(2n+1)p,l} \\
 & = \sum_{n=0}^{\infty} b_n J'_n(kb) V_{n,l}, \quad l = 0, 1, \dots,
 \end{aligned} \tag{23}$$

where

$$\begin{aligned}
 U_{m,l} &= \int_{-\beta}^{\beta} \cos m\theta \cos l\theta d\theta \\
 &= \begin{cases} 2\beta, & m = l = 0 \\ \frac{\sin(2m\beta)}{2m} + \beta, & m = l \neq 0 \\ \frac{\sin(m+l)\beta}{m+l} + \frac{\sin(m-l)\beta}{m-l}, & m \neq l \end{cases}
 \end{aligned} \tag{24}$$

$$\begin{aligned}
 V_{m,l} &= \int_{-\beta}^{\beta} \sin m\theta \sin l\theta d\theta \\
 &= \begin{cases} 0, & m = l = 0 \\ -\frac{\sin(2m\beta)}{2m} + \beta, & m = l \neq 0 \\ -\frac{\sin(m+l)\beta}{m+l} + \frac{\sin(m-l)\beta}{m-l}, & m \neq l \end{cases}
 \end{aligned} \tag{25}$$

All necessary formula derivation has been completed. By truncating the infinite term, the matrix is established to solve the unknown coefficients in the wave field expression, so as to carry out the subsequent case analysis.

4 Numerical results

We define the dimensionless frequency of incident waves as

$$\eta = 2a/\lambda = ka/\pi, \tag{26}$$

where λ is the wavelength of the incident waves. The dimensionless frequency λ can be used not only to

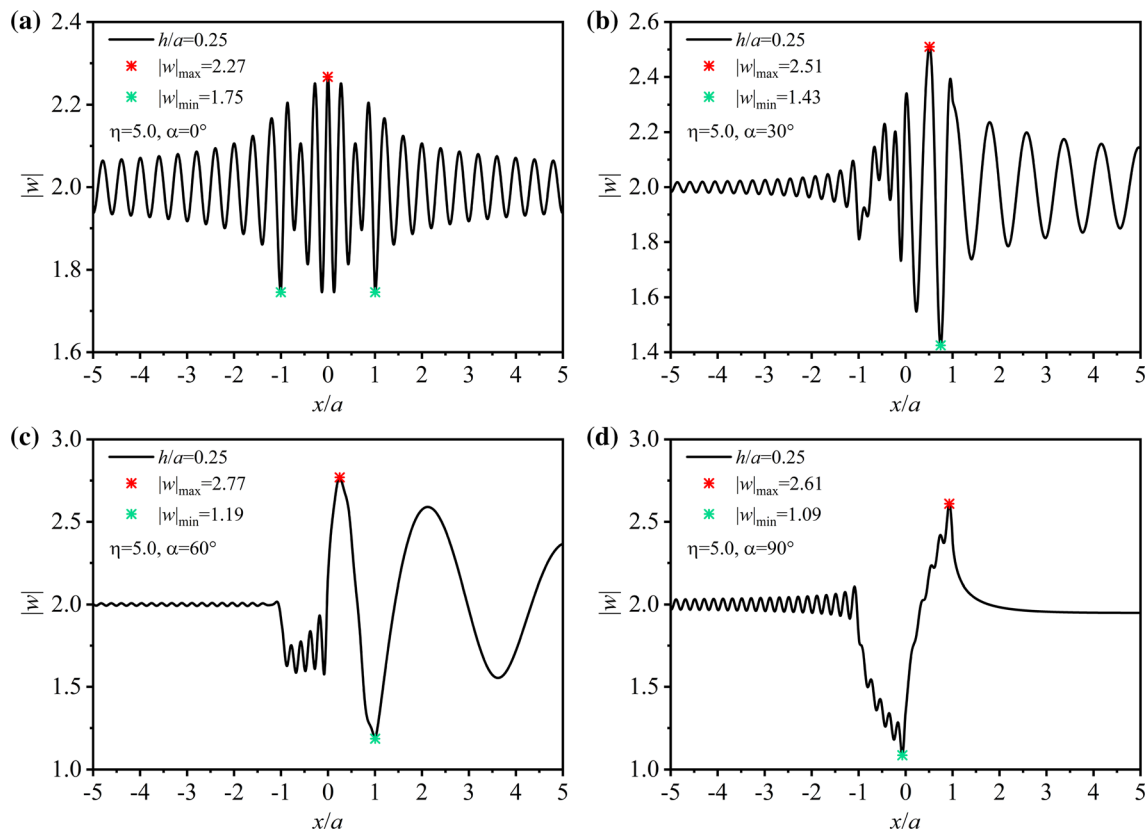


Fig. 7 Displacement amplitudes versus x/a for $h/a = 0.25$ at $\eta = 5.0$

characterize the ratio of the span of the triangle hill to the wavelength, but also to represent the magnitude of the wavenumber. The displacement amplitude which is used to characterize the magnitude of ground motion, is defined as

$$|w_j| = \sqrt{(\text{Re}w_j)^2 + (\text{Im}w_j)^2} \tag{27}$$

4.1 Convergence test

A number of convergence tests are carried out to determine the truncation values of n , m , l . Generally, more terms of n and l are required for higher dimensionless frequency of incident waves. For the number of truncation terms of m , 150 is enough to get the convergence results of the examples in this paper. Successive tests suggest that the horizontally incident cases take more truncation terms than others to reach convergence. In other words, as long as the displacement amplitudes converge in the case of $\alpha = 90^\circ$, the truncation term is sufficient for other incident angles. Take the case of $h/a = 0.4$ as an example. Figure 2a shows the five test positions where $S_1 - S_5$ are located at $x/a = -2.0, -0.5, 0, 0.5$ and 2.0 , respectively. The convergence of the displacement amplitudes of the five test

positions at three different dimensionless frequencies is shown in Fig. 2b–d. The abscissa N represents the truncation values of n and l . The displacement amplitudes of five positions need N to reach a certain value before they tend to be stable. Before that, the displacement amplitudes all present irregular and violent oscillations, so the results of non-convergence cannot be adopted. Although the positions of the five observation points are different, their convergence trend of displacement amplitude is similar. When the dimensionless frequency η is 5.0, the amplitude of the displacement is stabilized as N increases to 19. For high-frequency case with $\eta = 10.0$ and $\eta = 15.0$, the corresponding N when the displacement amplitudes begin to stabilize are 35 and 50, respectively.

4.2 Correctness verification

Qiu and Liu [12] have derived the correct wave field expressions of the isosceles triangle hill by complex function method. Although the numerical results given in this paper are not satisfactory for the most part, the displacement amplitudes of the shallow hill under low-frequency incidence can still be adopted as a reference under low-frequency incidence. In this paper, the method of

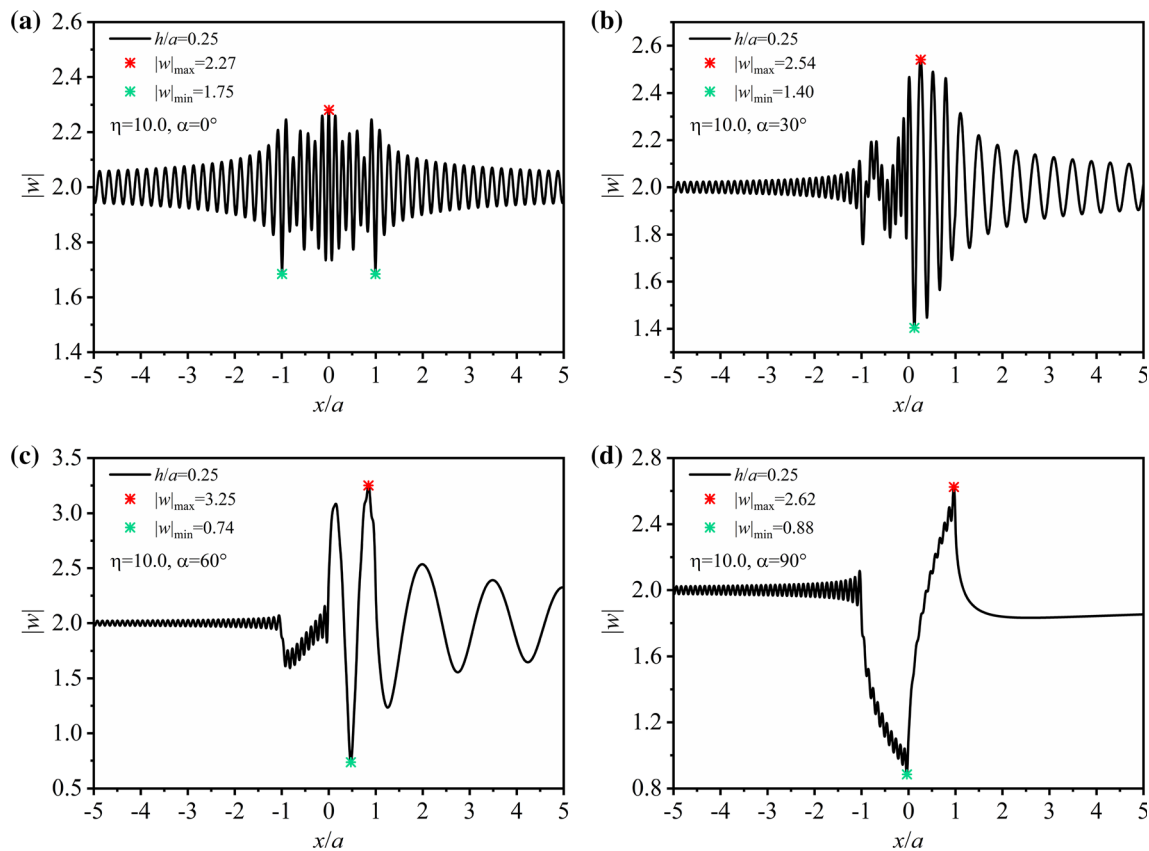


Fig. 8 Displacement amplitudes versus x/a for $h/a = 0.25$ at $\eta = 10.0$

model establishment and coefficient solution are different from that adopted by Qiu and Liu [12]. We set the hill height $h/a = 0.25, 0.5, 0.75$. Figure 3a shows the displacement amplitudes at vertical incidence with the dimensionless frequency $\eta = 0.5$ and Fig. 3b represents the case of oblique incidence. It can be seen that the results of present work are in good agreement with the results in Ref. [12]. The results obtained by the two different methods are basically coincident with each other, so it can be considered that the research method in this paper is effective.

To verify the accuracy of the numerical results obtained by the proposed model and method under the high-frequency incident SH waves, the finite element method is used for comparison. The height of the triangle hill is set as $h/a = 1.0$. The dimensionless frequency is $\eta = 5.0$, and seismic wave is incident from two different angles ($\alpha = 0^\circ$ and 30°). A comparison is performed to validate the solution results with those by the finite element method as shown in Fig. 4. The solid lines are the results obtained by the series solution in this paper, and the scatter points of the triangle are the results obtained by the finite element method. It can be seen that due to the limitation of the mesh division and the size of the solution domain, the results of the finite element method have errors, which

cannot be completely consistent with the analytical results in this paper. But the distribution trend of displacement amplitude is consistent, which can prove that the results obtained by this method in the case of high-frequency incident SH wave are effective.

4.3 Surface motion analysis

Figures 5 and 6 show the displacement amplitudes $|w|$ as a function of the distance x/a for $\eta = 1.0$ at various incident angles ($\alpha = 0^\circ, 30^\circ, 60^\circ, 90^\circ$). Set the dimensionless frequency equal to the span of the hill, i.e., $\eta = 1.0$. The effect of the triangle height on displacement amplitudes is considered when the ratio of hill height to span is less than 1.0 (shallow case) and greater than 1.0 (deep case). In Fig. 5, four cases of the height of hill are analyzed, which are $h/a = 0.2, 0.4, 0.6$ and 0.8 , respectively. Despite the different angles of incidence, the surface displacement amplitudes show a general rule. That is, a higher hill corresponds to a larger oscillation range of displacement amplitude. In the case of vertical incidence, the maximum displacement amplitude $|w|_{\max}$ corresponding to the four heights of the hill appears at the hilltop, and the minimum value $|w|_{\min}$ appears at the hillside. As the incident angle

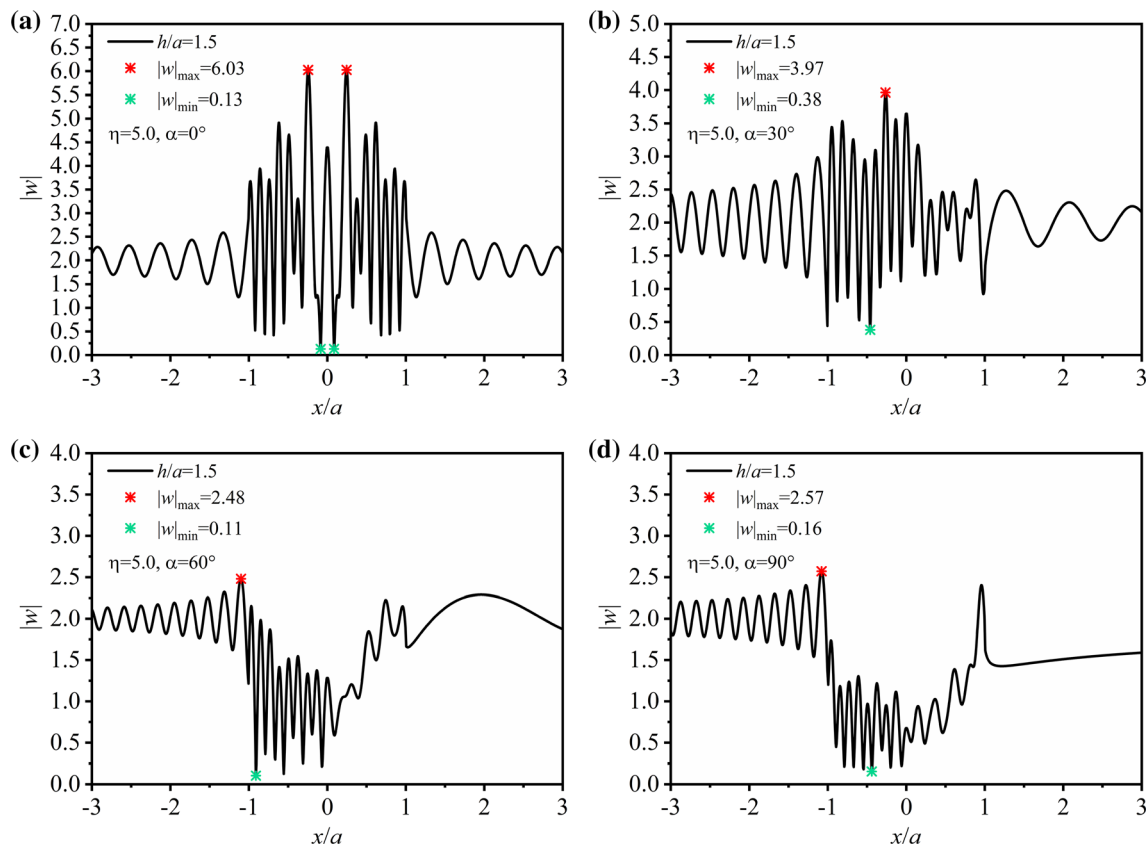


Fig. 9 Displacement amplitudes versus x/a for $h/a = 1.5$ at $\eta = 5.0$

increases, the positions of $|w|_{\max}$ and $|w|_{\min}$ shift from the original position to the right. Generally, extreme values of displacement amplitude occur on the surface of the isosceles triangle hill.

For deep hill, the displacement amplitudes at four incident angles are investigated when the height of the hill is set as $h/a = 1.2, 1.4, 1.6$ and 1.8 , respectively. When the dimensionless frequency is 1.0, the rule of surface displacement amplitudes corresponding to different hill height are quite different from that of shallow case. For the deep triangle hill, the influence of the height on the displacement amplitudes is not obvious. In the case of vertical incidence, although the maximum displacement amplitude of higher hill is larger, the increment of amplitude is slight. With the increase of incident angle, the influence of hill height on displacement amplitude is weakened, which is especially reflected in the left part of the surface ($x/a < 0$). It is worth noting that the maximum surface displacement amplitude $|w|_{\max}$ occurs on the horizontal surface to the left of the hill when $\alpha = 60^\circ$ and 90° .

After analyzing the surface displacement of the triangle hills with various heights under the low-frequency incident, the ground motion of the triangle hill at high dimensionless frequency is further analyzed in Figs. 7, 8, 9 and 10. The displacement amplitudes of the triangle hill with height of

0.25 and 1.5, respectively, at four incident angles ($\alpha = 0^\circ, 30^\circ, 60^\circ, 90^\circ$) are given, and the maximum and minimum values of the amplitudes in each case are marked out.

For vertical incidence ($\alpha = 0^\circ$) in Figs. 7a and 8a, the maximum ground motion occurs at the hilltop ($x/a = 0$) while the minimum one is at two rims of the hill ($x/a = \pm 1.0$). In this case, the displacement amplitude of the hill surface is generally greater than that of the flat surface on both sides. For oblique incidence ($\alpha = 30^\circ, 60^\circ$) in Figs. 7b, c and 8b, c, the position of the maximum displacement amplitude is shifted to the right-hand side, but it is still on the surface of the hill. When the seismic wave is incident at 60° , the corresponding maximum displacement amplitude reaches 2.77 at $\eta = 5.0$ and 3.25 at $\eta = 10.0$. It is noted that with the increase of the incident angle, the oscillation frequency of the ground displacement on the left side of the hill ($x/a < -1.0$) increases, but the oscillation amplitude decreases. However, the motion pattern on the right side of the hill ($x/a > 1.0$) is the opposite of the one on the left. And the displacement amplitude of the left hillside is obviously lower than that of the right hillside. For horizontal incidence ($\alpha = 90^\circ$) in Figs. 7d and 8d, the distribution of displacement results shows an obvious characteristic. That is, the amplification effect of triangular hill on seismic waves is mainly reflected on the

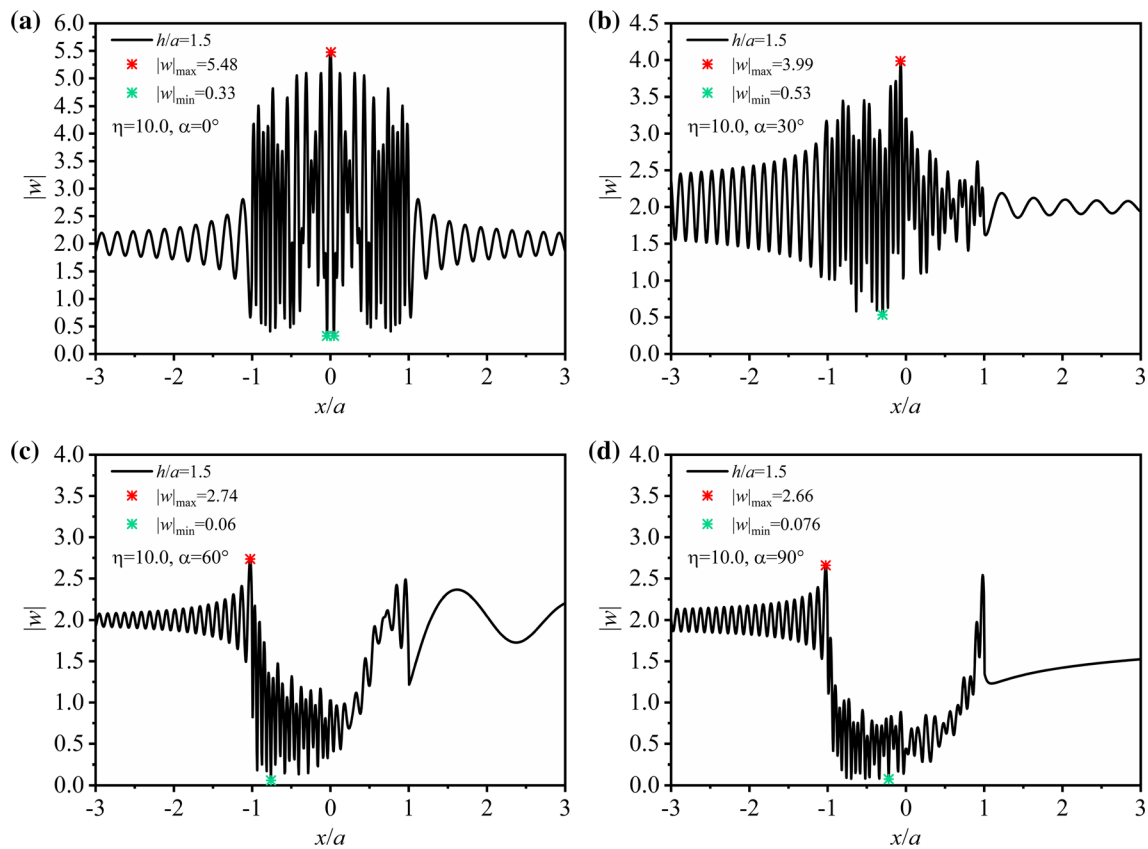


Fig. 10 Displacement amplitudes versus x/a for $h/a = 1.5$ at $\eta = 10.0$

right-side slope, while the ground motion on the left-side slope is obviously weakened. It is noted that this rule is just opposite to the result of V-shaped canyon in Ref. [17].

In order to analyze the surface displacement amplitudes of deep hill at high-frequency incidence, we set the hill height as $h/a = 1.5$, dimensionless frequency as $\eta = 5.0$ in Fig. 9 and $\eta = 10.0$ in Fig. 10. Compared with the cases of low frequency, the amplitude distribution of ground displacement under high-frequency incidence is much more complex. To show the displacement amplitude of the hill surface ($-1.0 \leq x/a \leq 1.0$) more clearly, we reduce the abscissa interval to $(-3.0, 3.0)$. For vertical incidence, the maximum and minimum amplitudes still occur near the top of the hill, and the amplification effect of the amplitude is significant. In the two examples, the maximum amplitude reaches 6.03 at the frequency of 5.0. With the increase of incident angle α , the displacement amplitudes of the hill surface decrease. When the incident angle is 60° and 90° , the initial amplification effect (while $\alpha = 0^\circ, 30^\circ$) of the hill on the seismic wave energy changes to the shielding effect. This shielding effect is reflected in the displacement amplitudes of the hill surface are obviously less than 2.0, and the displacements of the flat surface on the right side of the hill also have a certain reduction. The closer to grazing

incidence ($\alpha = 90^\circ$), the more obvious the shielding effect is. In addition, large incident angle makes the maximum displacement amplitude occur at the left rim of the hill.

Figure 11 illustrates the displacement amplitudes $|w|$ as a function of the dimensionless frequency η at two incident angles ($\alpha = 60^\circ, 90^\circ$). Five observer points are selected to study the displacement amplitudes of five typical locations as shown in Fig. 11a in a large frequency interval. For point 1, the displacement amplitudes under low-frequency incident corresponding to the two incident angles are basically the same. As the dimensionless frequency increases, the difference in displacement amplitude at two incident angles becomes apparent. The displacement amplitudes fluctuate regularly with the dimensionless frequency and are always less than 2.0. For point 2 and point 3, the displacement amplitudes are less than 2.0 at 60° incidence, and they decrease with the increase of dimensionless frequency η . In contrast, the displacements of oblique incidence are significantly larger than that of horizontal incidence. The magnifying effect of the hill on the seismic wave is reflected in the right part of the triangle hill at $\alpha = 90^\circ$. As shown in Fig. 11e, f, the black curve presents an upward trend and is always greater than 2.0. The displacement of the right rim of the hill at the horizontal

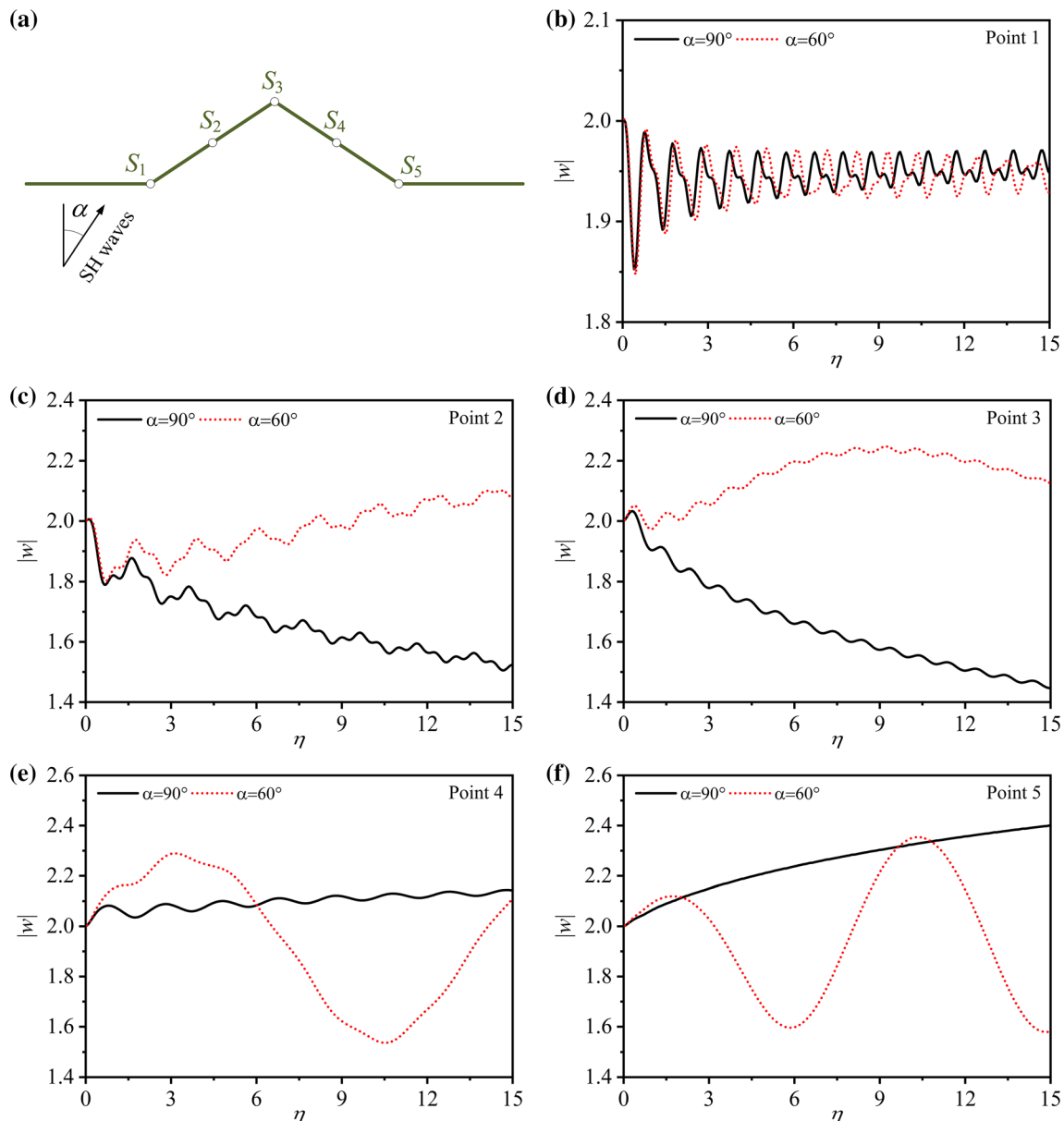


Fig. 11 Five observer points' seismic responses versus η at $h/a = 0.1$ for two incident angles

incidence of SH wave is significantly larger than that at the oblique incidence.

Figure 12 is presented to show the displacement amplitudes of a deep hill versus dimensionless frequency η . We find that the oscillation forms of displacement amplitudes are similar under two incident angles ($\alpha = 60^\circ, 90^\circ$), which is different from the case of shallow hill. For the observer points on hillside and hilltop, in general, the surface displacements caused by oblique incidence of SH waves are larger than that of grazing incidence. This means that for the deep hill, a larger incident angle corresponds to a more significant earthquake wave energy absorption effect, which is applicable to the whole frequency range

($0 < \eta \leq 15$). With regard to observer point 1 at the left rim of the deep hill, the oscillation range of displacement amplitudes under oblique incidence ($\alpha = 60^\circ$) is larger than that under grazing incidence ($\alpha = 90^\circ$). And the displacement amplitude of point 1 is larger than that of other locations, which indicates that this point may be an earthquake risk position that needs attention. Compared with shallow hill, the ground motion response of deep hill is much more complex, and with the increase of dimensionless frequency, the distribution of ground displacement amplitude has no obvious regularity.

For the sake of revealing the influence of dimensionless frequency η and incident angle α on surface motions,

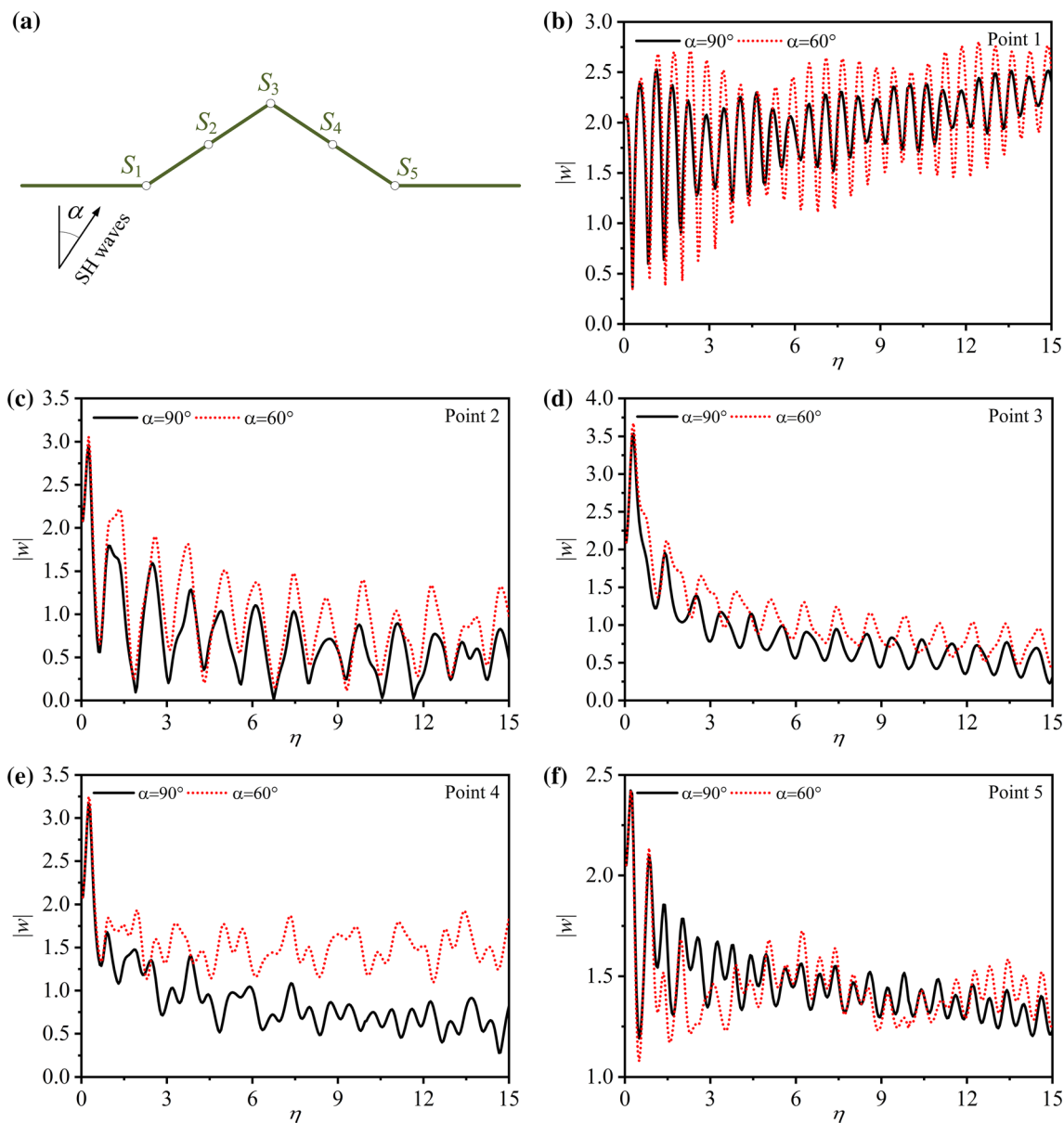


Fig. 12 Five observer points' seismic responses versus η at $h/a = 1.5$ for two incident angles

Fig. 13 displays the displacement amplitudes as a function of x/a and η at various angles of incidence ($\alpha = 90^\circ, 60^\circ, 30^\circ, 0^\circ$). We set $h/a = 0.25$. Surface motion around the triangle hill under horizontal incidence ($\alpha = 90^\circ$) is shown in Fig. 13a. It can be seen intuitively that at any dimensionless frequency, the displacement oscillation of the flat surface on the right side of the hill ($x/a > 1.0$) is gentle, while that on the left side ($x/a < 1.0$) is violent. For oblique incidence, the maximum amplitude of surface displacement generally occurs around the right foot of the hill ($x/a = 1.0$), and the ground motion of the flat surface on the right side ($x/a > 1.0$) is significantly stronger than that on the left ($x/a < 1.0$). At vertical incidence, the ground motion on both sides is the same because of the

symmetrical shape of the triangle hill. Maximum displacement amplitude occurs on the hill surface ($-1.0 \leq x/a \leq 1.0$).

5 Conclusion

In this paper, an exact solution using wave-function series expansion method for the scattering of SH waves by an isosceles triangle hill has been presented. By introducing the fractional Bessel function, the expression of standing wave field satisfying the stress-free condition in polar coordinate system is constructed. The research method proposed in this paper is applicable for isosceles triangle

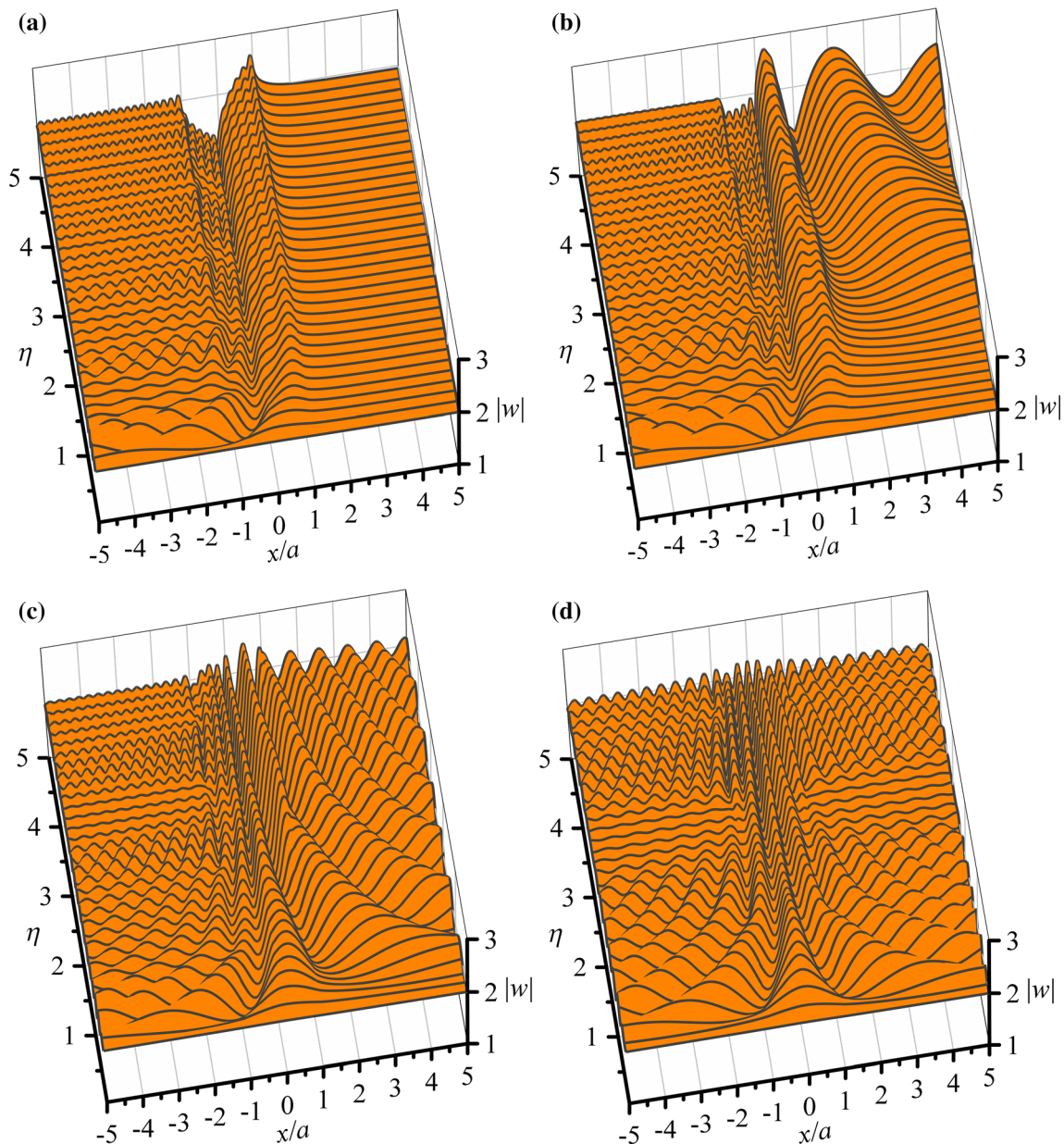


Fig. 13. 3D plots of surface displacement amplitudes around the isosceles triangle hill for $h/a = 0.25$ at different incident angles

hill with arbitrary height. Based on the orthogonality of trigonometric functions, the infinite algebraic equations for solving coefficients are derived. The numerical results are accurate and convergent in spite of high-frequency incidence. According to the foregoing analysis, some findings can be summarized as follows:

1. Steeper hill makes more complex ground motion responses. For small incident angle, the amplification effect of deep hill is more obvious than that of shallow hill.
2. The position of the maximum displacement is affected by the incident angle. In the case of vertical and

horizontal incidence, the maximum displacement amplitude $|w|_{\max}$ appears at the hill top ($x/a = 0$) and at the left rim of the hill, respectively.

3. Once the incident angle is greater than 45° , the displacement of the hill surface decreases, and the triangle hill has a barrier effect on seismic waves.
4. The method presented in this paper is applicable for the further study of the scattering of SH waves by non-isosceles triangular hill.

Acknowledgements This work is supported by the National Key Research and Development Program of China (Grant No.

2019YFC1509301), the National Natural Science Foundation of China (Grant No. 11872156), the Fundamental Research Funds for the Central Universities and the program for Innovative Research Team in China Earthquake Administration.

References

- Abramowitz M, Stegun IA (1964) Handbook of mathematical functions, with formulas, graphs and mathematical tables. National Bureau of Standards, Washington
- Amornwongpaibun A, Lee VW (2013) Scattering of anti-plane (SH) waves by a semi-elliptical hill: II—deep hill. *Soil Dyn Earthq Eng* 52:126–137. <https://doi.org/10.1016/j.soildyn.2012.08.006>
- Chang KH, Tsaur DH, Wang JH (2013) Scattering of SH waves by a circular sectorial canyon. *Geophys J Int* 195:532–543. <https://doi.org/10.1093/gji/ggt236>
- Chang KH, Tsaur DH, Wang JH (2015) Response of a shallow asymmetric V-shaped canyon to antiplane elastic waves. *Proc R Soc A Math Phys Eng Sci* 471:20140215. <https://doi.org/10.1098/rspa.2014.0215>
- Chen JT, Chen PY, Chen CT (2008) Surface motion of multiple alluvial valleys for incident plane SH-waves by using a semi-analytical approach. *Soil Dyn Earthq Eng* 28:58–72. <https://doi.org/10.1016/j.soildyn.2007.04.001>
- Chen X, Zhang N, Gao YF, Dai DH (2019) Effects of a V-shaped canyon with a circular underground structure on surface ground motions under SH wave propagation. *Soil Dyn Earthq Eng*. <https://doi.org/10.1016/j.soildyn.2019.105830>
- Gao YF, Zhang N, Li DY, Liu HL, Cai YQ, Wu YX (2012) Effects of topographic amplification induced by a U-shaped canyon on seismic waves. *Bull Seismol Soc Am* 102:1748–1763. <https://doi.org/10.1785/0120110306>
- Hayir A, Todorovska MI, Trifunac MD (2001) Antiplane response of a dike with flexible soil-structure interface to incident SH waves. *Soil Dyn Earthq Eng* 21:603–613. [https://doi.org/10.1016/S0267-7261\(01\)00035-5](https://doi.org/10.1016/S0267-7261(01)00035-5)
- Lee VW, Amornwongpaibun A (2013) Scattering of anti-plane (SH) waves by a semi-elliptical hill: I—shallow hill. *Soil Dyn Earthq Eng* 52:116–125. <https://doi.org/10.1016/j.soildyn.2012.08.005>
- Lee VW, Luo H, Liang JW (2006) Antiplane (SH) waves diffraction by a semicircular cylindrical hill revisited: an improved analytic wave series solution. *J Eng Mech* 132:1106–1114. [https://doi.org/10.1061/\(asce\)0733-9399\(2006\)132:10\(1106\)](https://doi.org/10.1061/(asce)0733-9399(2006)132:10(1106))
- Liang JW, Fu J (2011) Surface motion of a semi-elliptical hill for incident plane SH waves. *Earthq Sci* 24:447–462. <https://doi.org/10.1007/s11589-011-0807-1>
- Qiu FQ, Liu DK (2005) Antiplane response of isosceles triangular hill to incident SH waves. *Earthq Eng Eng Vibration* 4:37–46. <https://doi.org/10.1007/s11803-005-0022-y>
- Shyu WS, Teng TJ (2014) Hybrid method combines transfinite interpolation with series expansion to simulate the anti-plane response of a surface irregularity. *J Mech* 30:349–360. <https://doi.org/10.1017/jmech.2014.27>
- Song YQ, Li XZ, Yang Y, Sun MH, Yang ZL, Fang XQ (2020) Scattering of anti-plane (SH) waves by a hill with complex slopes. *J Earthq Eng*. <https://doi.org/10.1080/13632469.2020.1767231>
- Sánchez-Sesma FJ, Herrera I, Avilés J (1982) A boundary method for elastic wave diffraction: application to scattering of SH waves by surface irregularities. *Bull Seismol Soc Am* 72:473–490
- Trifunac MD (1973) Scattering of plane SH waves by a semi-cylindrical canyon. *Earthq Eng Struct Dyn* 1:267–281. <https://doi.org/10.1002/eqe.4290010307>
- Tsaur DH, Chang KH (2008) An analytical approach for the scattering of SH waves by a symmetrical V-shaped canyon: shallow case. *Geophys J Int* 174:255–264. <https://doi.org/10.1111/j.1365-246X.2008.03788.x>
- Tsaur DH, Chang KH (2009) Scattering and focusing of SH waves by a convex circular-arc topography. *Geophys J Int* 177:222–234. <https://doi.org/10.1111/j.1365-246X.2008.04080.x>
- Tsaur DH, Chang KH, Hsu MS (2010) An analytical approach for the scattering of SH waves by a symmetrical V-shaped canyon: deep case. *Geophys J Int* 183:1501–1511. <https://doi.org/10.1111/j.1365-246X.2010.04806.x>
- Yang ZL, Jiang GXX, Sun C, Tang TS, Yang Y (2019) The role of soil anisotropy on SH wave scattering by a lined circular elastic tunnel in an elastic half-space soil medium. *Soil Dyn Earthq Eng* 125:105721. <https://doi.org/10.1016/j.soildyn.2019.105721>
- Yang ZL, Li XZ, Song YQ, Jiang GXX, Yang Y (2019) Scattering of SH waves by a semi-cylindrical canyon in a radially inhomogeneous media. *Waves Random Complex Media*. <https://doi.org/10.1080/17455030.2019.1649741>
- Yang ZL, Song YQ, Li XZ, Jiang GXX, Yang Y (2020) Scattering of plane SH waves by an isosceles trapezoidal hill. *Wave Motion* 92:102415. <https://doi.org/10.1016/j.wavemoti.2019.102415>
- Yao Y, Wang R, Liu TY, Zhang JM (2018) Seismic response of high concrete face rockfill dams subjected to non-uniform input motion. *Acta Geotech* 14:83–100. <https://doi.org/10.1007/s11440-018-0632-y>
- Yuan XM, Liao ZP (1994) Scattering of plane SH waves by a cylindrical canyon of circular-arc cross-section. *Soil Dyn Earthq Eng* 13:407–412. [https://doi.org/10.1016/0267-7261\(94\)90011-6](https://doi.org/10.1016/0267-7261(94)90011-6)
- Yuan XM, Liao ZP (1996) Surface motion of a cylindrical hill of circular-arc cross-section for incident plane SH waves. *Soil Dyn Earthq Eng* 15:189–199. [https://doi.org/10.1016/0267-7261\(95\)00040-2](https://doi.org/10.1016/0267-7261(95)00040-2)
- Yuan XM, Men FL (1992) Scattering of plane SH waves by a semi-cylindrical hill. *Earthq Eng Struct Dyn* 21:1091–1098. <https://doi.org/10.1002/eqe.4290211205>
- Zhang N, Gao YF, Cai YQ, Li DY, Wu YX (2012) Scattering of SH waves induced by a non-symmetrical V-shaped canyon. *Geophys J Int* 191:243–256. <https://doi.org/10.1111/j.1365-246X.2012.05604.x>
- Zhang N, Zhang Y, Gao YF, Pak RYS, Wu YX, Zhang F (2019) An exact solution for SH-wave scattering by a radially multi-layered inhomogeneous semi-cylindrical canyon. *Geophys J Int* 217:1232–1260. <https://doi.org/10.1093/gji/ggz083/5319212>
- Zhang N, Zhang Y, Gao YF, Pak RYS, Yang J (2019) Site amplification effects of a radially multi-layered semi-cylindrical canyon on seismic response of an earth and rockfill dam. *Soil Dyn Earthq Eng* 116:145–163. <https://doi.org/10.1016/j.soildyn.2018.09.014>

Publisher's Note Springer Nature remains neutral with regard to jurisdictional claims in published maps and institutional affiliations.